LAND SUBSIDENCE IN COASTAL TEXAS: LOCATIONS, RATES, TRIGGERS, AND CONSEQUENCES

A Thesis

by

MICHAEL HALEY

BS, Texas A&M University – Corpus Christi, 2019

Submitted in Partial Fulfillment of the Requirements for the Degree of

MASTER OF SCIENCE

in

ENVIRONMENTAL SCIENCE

Texas A&M University-Corpus Christi
Corpus Christi, Texas

August 2021

August 2021

LAND SUBSIDENCE IN COSTAL TEXAS: LOCATIONS, RATES, TRIGGERS, AND CONSEQUENCES

A Thesis

by

MICHAEL HALEY

This thesis meets the standards for scope and quality of
Texas A&M University-Corpus Christi and is hereby approved.

Ahmed Mohamed, PhD
Chair

Dorina Murgulet, PhD
Committee Member

Michael Starek, PhD
Committee Member

August 2021

ABSTRACT

Land subsidence and sea level rise are well-known ongoing problems that are negatively impacting the entire Texas coast. While ground-based monitoring techniques using Global Positioning System (GPS) provide accurate subsidence rates, they are labor intensive, expensive, time consuming, and spatially limited (e.g., point measurements). In this study, Interferometric Synthetic Aperture Radar (InSAR) techniques were used to map locations and quantify rates of land subsidence in the Texas Costal Bend region during the period from October 2016 to July 2019. InSAR-derived land subsidence rates were validated against GPS-derived rates. Factors controlling the observed land subsidence rates and locations were also investigated. Consequences of increased land subsidence rates in Texas Costal Bend region were examined. Results indicate: (1) land subsidence rates in the Coastal Bend exhibit both spatial and temporal variabilities, (2) some areas experienced a localized subsidence as high as -21 mm/yr and other areas show a land uplift with rate of > 10 mm/yr, (3) InSAR-derived land subsidence rates were consistent with GPS-derived deformation rates, (4) Seven regions (e.g., Victoria, George West, Refugio, Falfurrias, Karnes City, McAllen, and Nueces Bay/Corpus Christi) were observed to experience significant land subsidence rates along Texas Costal Bend region during the investigated period, (5) land subsidence in Coastal Texas is attributed mainly to oil and ground water extraction as well as vertical movements along growth faults, and (6) land subsidence increased both flood frequency and severity in Coastal Texas. Our results provide valuable information regarding not only land deformation rates in the Texas Coastal Bend region, but alsothe effectiveness of interferometric techniques in other coastal rural areas around the world that lack significant GPS coverage. Mapping land subsidence rates and locations in coastal Texas

significantly improve the current understanding of factors controlling the variability in land deformation in coastal areas by providing a high-resolution spatial and temporal dataset that is currently not available on this detailed scale.

ACKNOWLEDGEMENTS

First, I would like to thank my advisor Dr. Mohamed Ahmed for the immense amount of support, encouragement, advice, and patience that he showed during my graduate studies. I am truly grateful to say that not only has he made me a better scientist throughout this process, but truly a better person. Second, I would like to thank my committee members Dr. Dorina Murgulet and Dr. Michael Starek, without their support and expert inputs, this study would not be possible. I have truly had a wonderful committee that have pushed me to reach and surpass my goals and I will forever be grateful for this.

This research was supported by the Division of Research and Innovation at Texas A&M University – Corpus Christi (Texas Comprehensive Research Funds and Research Equipment and Infrastructure Grant).

TABLE OF CONTENTS

LIST OF FIGURES

FIGURE PAGE

LIST OF TABLES

TABLES PAGE

CHAPTER I

Introduction

1. Background

Currently, more than 30% of the world's population lives in coastal areas, and 50% are expected to do so by 2030 (Small and Nicholls 2003). However, the majority of coastal areas are witnessing land subsidence (Abidin et al. 2013; Eggleston and Pope 2013; Blackwell et al. 2020). Land subsidence increases vulnerability of coastal communities to natural forces such as flooding, hurricanes, tsunamis, and sea-level rise (Wu et al. 2002; Dolan and Walker 2006; Felsenstein and Lichter 2014). Hurricanes and flooding are associated with loss of life, livestock,crops, and natural habitat; property damage; and contamination of surface and groundwater resources (Grineski et al. 2019; Venkataramanan et al. 2019). Sea-level rise is usually associated with inundation of wetlands and deltas, enhanced coastal erosion, increased vulnerability ofcostal environments to storms, and seawater intrusion/pollution in coastal aquifers and surface water supplies (Don et al. 2006; Fitzgerald et al. 2008).

Land subsidence and sea level rise are ongoing phenomena that negatively impact the entire Texas coast (Bawden et al. 2012). In Texas, land subsidence is generally attributed mainly to sediment compaction, faulting, salt tectonics, and fluid (groundwater and hydrocarbon) withdrawal (Zilkoski et al. 2003; Khan et al. 2014; Qu et al. 2015a).

Although ground-based monitoring techniques such as the global positioning system(GPS) stations provide accurate land subsidence rates, they are labor intensive, expensive, time consuming, and spatially limited (in other words, they are point measurements) (Paine 1993; Zilkoski et al. 2003). The use of radar interferometry offers an alternative solution to this problem by providing land deformation rates on a spatially global scale.

Synthetic Aperture Radar (SAR) is a technique that uses temporal radar images to infer topographic relief as well as subtle topographic changes. The main principle of SAR is that the longer an antenna is the higher the resolution of the observed surface features will be. Due to limitations in antenna sizes on spaceborne satellites, SAR was created to give the effect of a larger antenna with a fixed antenna length. This is done by the satellite sending pulsed signals at regular intervals of the same surface features and receives them give the effect of increasing the length of the antenna and thus the name Synthetic Aperture Radar (Shan and Ye 1998).

Interferometric Synthetic Aperture Radar (InSAR) takes advantages of the high-resolution SAR images by using mathematical manipulation to calculate millimeter scale deformation. First, a pair of overlapping SAR images must be acquired. This is done by a satellite mounted radar observing the same land feature at almost an identical vantage point at different times. The next step is to co-register the two images so that phase information can be generated from each pixel and paired with the corresponding pixel in the second image. The next step is creating interferograms which is done by subtracting the phase values from each corresponding pixel. Next, the effects of geometry and topography must be removed. Because the satellite takes each image acquisition from a slightly different vantage point, the viewing angle is slightly different on each image. This look angle difference causes a predictable interference patten that must be removed as it is not a product of the land deformation and is noise for InSAR studies. Topography is removed from the interferogram via a digital elevation model (DEM). Topography causes a predictable interference pattern based on the look angle and wavelength of the sensor. Lastly, a weather model correction is applied to remove any atmospheric noise that could be within the images. Atmospheric noise appears in the form of atmospheric delay anomalies that complicate the interpretation of the interferograms greatly.

These anomalies originate in the troposphere or ionosphere and are usually caused by inhomogeneities in water content, temperature or electron density (Dzurisin and Lu 2006)

Resulting interferograms represent changes only in distance between ground surface and the radar instrument. Distance changes are used to generate maps of land surface deformation over areas of interest (Hooper et al. 2007; Ferretti et al. 2011; Galloway and Burbey 2011; Milleret al. 2017; Gebremichael et al. 2018). Radar interferometric techniques have been successfully used to map and measure topographic variation rates as small as 0.1 mm/yr (Massonnet and Feigl1998), deformation and fault slip from earthquakes (Aslan et al. 2019), mine subsidence (Blachowski et al. 2019), aquifer compaction from pumping (Galloway et al. 1998; Othman et al.2018), landslides (Hu et al. 2019), and land subsidence in urban areas (Khan et al. 2014; Qu et al.2015b). InSAR studies have previously been effectively used in coastal areas around the world and even in the gulf coast, most notably in Houston.Qu et al. (2015) found that between in the 1990s and 2000s northwest Houston was experiencing subsidence rates as high as 53 mm/yr. Additionally, a strong spatial and temporal correlation was found between fluid withdrawal and subsidence in corresponding areas. They also reported that 8 hydrocarbon extraction fieldswithin the Houston area were seeing localized subsidence. Additionally, a heterogeneous land deformation was reported at different points along multiple faults within the Houston study area.

Bawden et al. (2012) found that the northwestern portions of Harris County were experiencing rapid subsidence. The subsidence is linked with large amounts of groundwater extraction. It is estimated that between 1900 and 1979 as much as 3 m of subsidence had occurred in areas of Houston. This study conducted an InSAR study in conjunction with the use of GPS for validation . These studies showed that the historical areas of subsidence had now slowed down, but the new feature of subsidence the “northwest subsidence feature” was the new

primary area of concern in the area. This study also showed that areas of previous subsidence due to groundwater extraction, could be regions of uplift with modern water conservationmethods and the replenishment of aquifers.

Miller and Shirzaei(2019) reported that between 2007 and 2011 northwest Houston was experiencing land subsidence rates of 24 – 30 mm/yr. However, between 2015 and 2017 subsidence rates as high as 24 mm/yr were observed again in northwest Harris County. This study also incorporated the use of SAR acquisitions to map flooding in Houston in the aftermath of hurricane Harvey and found that there was a significant correlation between areas that were inundated and land subsidence rates.

InSAR studies in coastal areas have also been used successfully in other parts of the United States. For example, Blackwell et al. (2020) found that that four major cities along the California coast: San Francisco Bay area, Monteerrey Bay, Los Angeles and San Diego were all experiencing subsidence. It notably found that in Los Angeles the observed subsidence rates were congruent with an increase in fluid extractions during the period and thus compaction of theunderlying strata. In San Francisco and Monterrey Bay the primary controlling factors appear to be the large amount of faulting in the area, notably the San Andreas fault system.

In Miami, and Norfolk, ,Fiaschi and Wdowinski (2020) found that subsidence in Miami, Florida coupled with an increase in sea level has caused more frequent flooding events most notably on south beach where the localized subsidence is observed. While in Norfolk, Virginia, higher average subsidence rates are seen throughout the entire study area and are spatially correlated with an increase in groundwater extraction activities.

We believe that the aforementioned studies show that InSAR is an effective technique to monitor land subsidence in a coastal environment. These prior studies point out faulting and fluid

extraction as primary controlling factors for land subsidence, and spatially correlating these two factors with observed land deformation rates from InSAR will help greatly in the understanding for the possible causes of land deformation within the Coastal Bend.

2. Objectives and Significance

In this study, radar interferometric techniques were used to map locations, quantify rates, investigates controlling factors, and examine the consequences of land subsidence in the Costal Bend region in Texas (Figure 1). This research will provide valuable information regarding not only land deformation rates in the Texas Coastal Bend region, but also the effectiveness of interferometric techniques in other coastal rural areas around the world that lack significant GPS coverage. Mapping land subsidence rates and locations in South Texas significantly improve the current understanding of factors controlling the variability in land deformation in coastal areas by providing a high-resolution spatial and temporal dataset that is currently not available on this scale. Additionally, most of the current models that are used to assess the impacts of sea level rise on coastal resiliency utilize constant, in space and time, land deformation rates. The results of this study could be used to improve the performance of many sea level rise impact models.

3. Study Area

The Coastal Bend region of Texas (Figure 1) represents our study area. Much of the study area is comprised of rural countryside and small towns, so conventional methods of tracking land deformation such as GPS (green dots; Figure 1) do not provide a spatially adequate dataset over the entire region because the GPS stations are concentrated in the larger towns within the region. Land cover in the study area is primarily agriculture and rangelands. The agriculture and urban

areas have been steadily growing in the area, while the forest, rangeland and wetland portions are all steadily shrinking (Stukey, Jared 2004).

Geologically, the Coastal Bend region is situated on a passive depositional margin with geologic formations consisting primarily of alternating sand, silt, and clay layers (Figure 2). The sedimentary sections are estimated to be 4,500 – 5,500 m thick near the coastline. These sedimantary sections are heavily faulted. The faulting tends to be regional, and varies in complexity from system to system (Baker 1995). Growth faults, parrallel to the coastline, are common within the Texas coast and are attributed to the loading on the unconsolidated sediments in this region (Ryder and Ardis 2002; Bruun et al. 2016). The faults are part of part of the Cenozoic Wilcox and Frio fault trends which are comprised of large displacement, dominantly down to the basin growth faults (Jackson et al. 2020). Fault density within the area is shown in figure 2b, showing the concentration of growth faults spatially within the area.

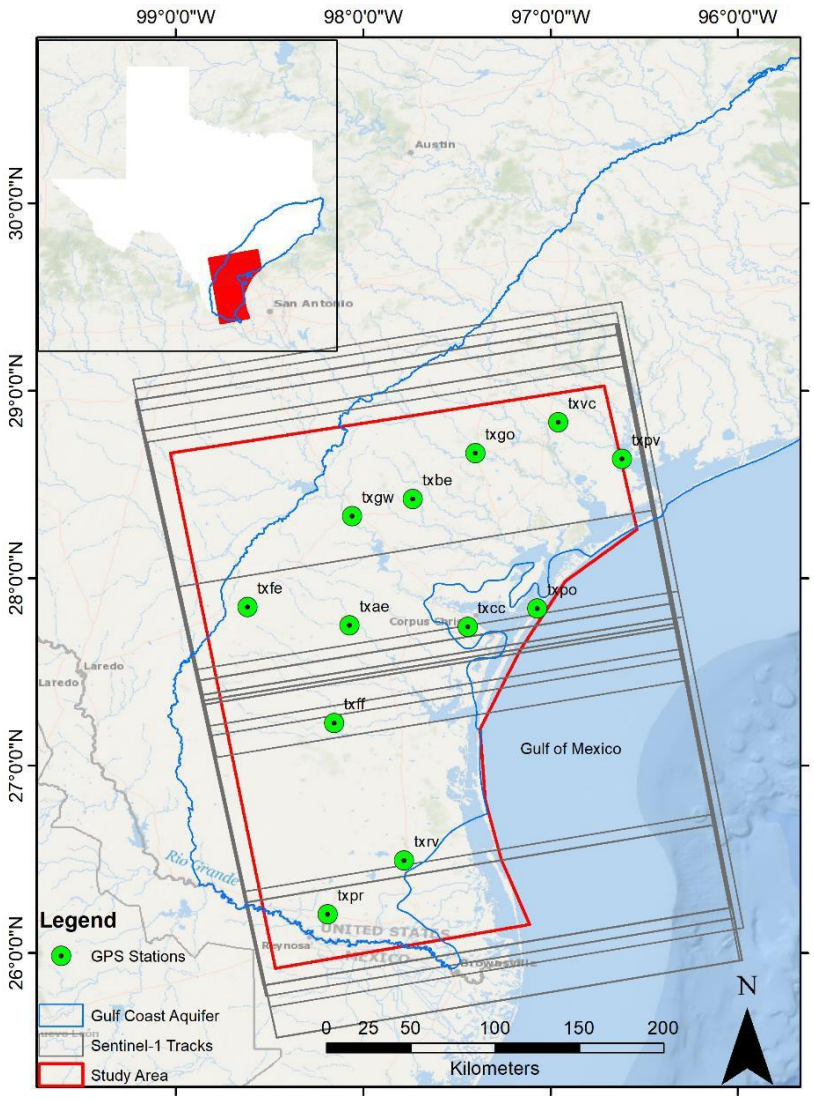

Figure 1: Map showing study area (red polygon), Sentinel-1 footprints (gray polygons), Gulf Coast Aquifer (blue polygon), and locations of GPS Stations (green circles).

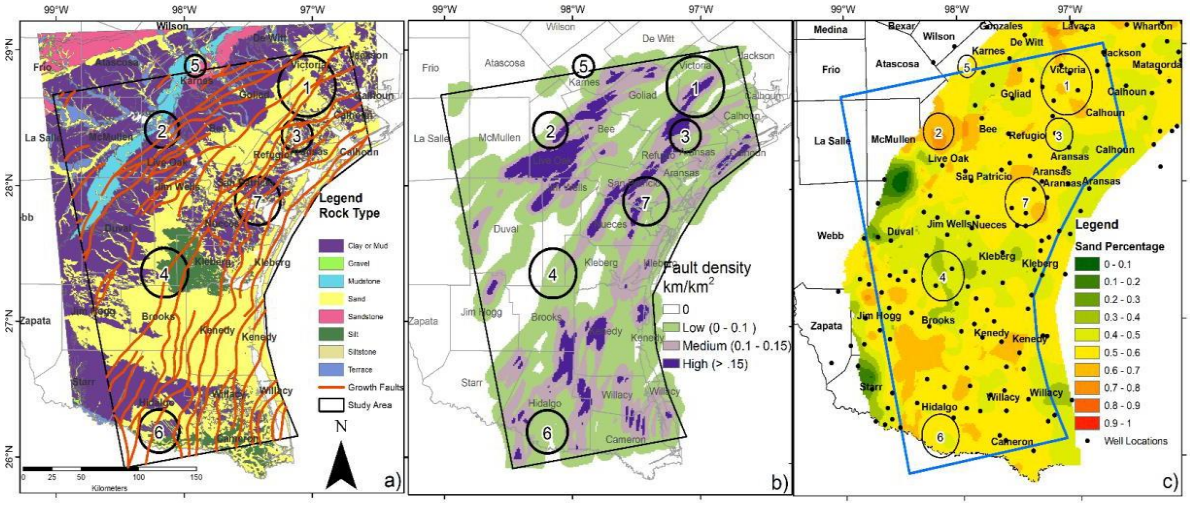

Figure 2: (a) Geologic map showing surface lithology within Texas Coastal Bend region. Also shown is the spatial distribution of growth faults (orange lines). (b) Growth faults density (in km/km^2) within the study area. (c) Spatial distribution of sand percentage within the GCA. Circles 1 to 7 are areas that were identified to witness a significant land subsidence during the investigated period.

The hydrogeology of the study area is dominated by the Gulf Coast Aquifer (GCA) system, which runs parallel to the Gulf of Mexico coastline from the Louisiana border in the northeast to the border with Mexico in the southwest. This GCA system contains several aquifersincluding: Jasper aquifer, Evangeline aquifer, and the Chicot aquifer. These aquifers are composed of discontinuous sand, silt, and clays. These aquifer units thicken toward the Gulf of Mexico (Chowdhury et al. 2001). Groundwater is typically unconfined or semi-confined in this system. The specific yields from GCA are quite low when compared to other sedimentary unconfined aquifer systems due to the interbedded silt/clay lenses that confine the aquifers in smaller areas (Chowdhury et al. 2004).

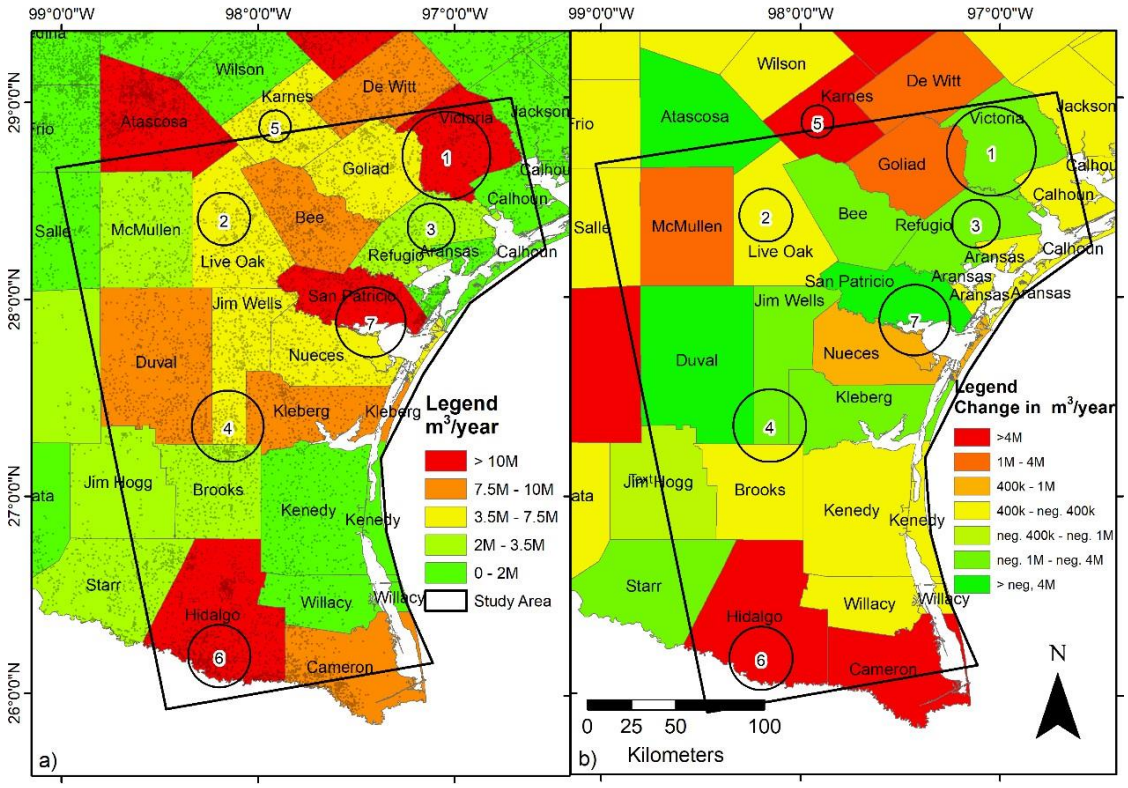

Figure 3: (a) Map showing historical groundwater extraction (in m^3/yr) averaged by county during the period from 2000 to 2015. (b) Difference between groundwater extraction (in m^3/yr) between the study period (2016-2019) and the historical period (2000-2015). Circles 1 to 7 are areas that were identified to witness a significant land subsidence during the investigated period.

The large volume of water pumped from the aquifers has caused subsidence, particularly in the Houston area (Bawden et al. 2012; Qu et al. 2015c); however, recent application of water conservation strategies has driven substantial water level rebounds. Groundwater extractionwithin the GCA is estimated at 518×10^9 m^3 per year. Most of the pumping in the area occurs in the form of irrigation (Chowdhury et al. 2004). Figure 3 shows spatial distribution of groundwater extraction rates in the Coastal Bend region.

Oil and Gas extraction practices are significant within the study area. Oil and gas extraction, along with the fluid injection that accompany it, have been shown to cause localized land deformation within oil and gas fields (Kim and Lu 2018). Figure 4 shows average annual oil extraction rates extracted from the Texas Railroad Commission (https://www.rrc.state.tx.us/) between January 1993 and January 2020 for each county.

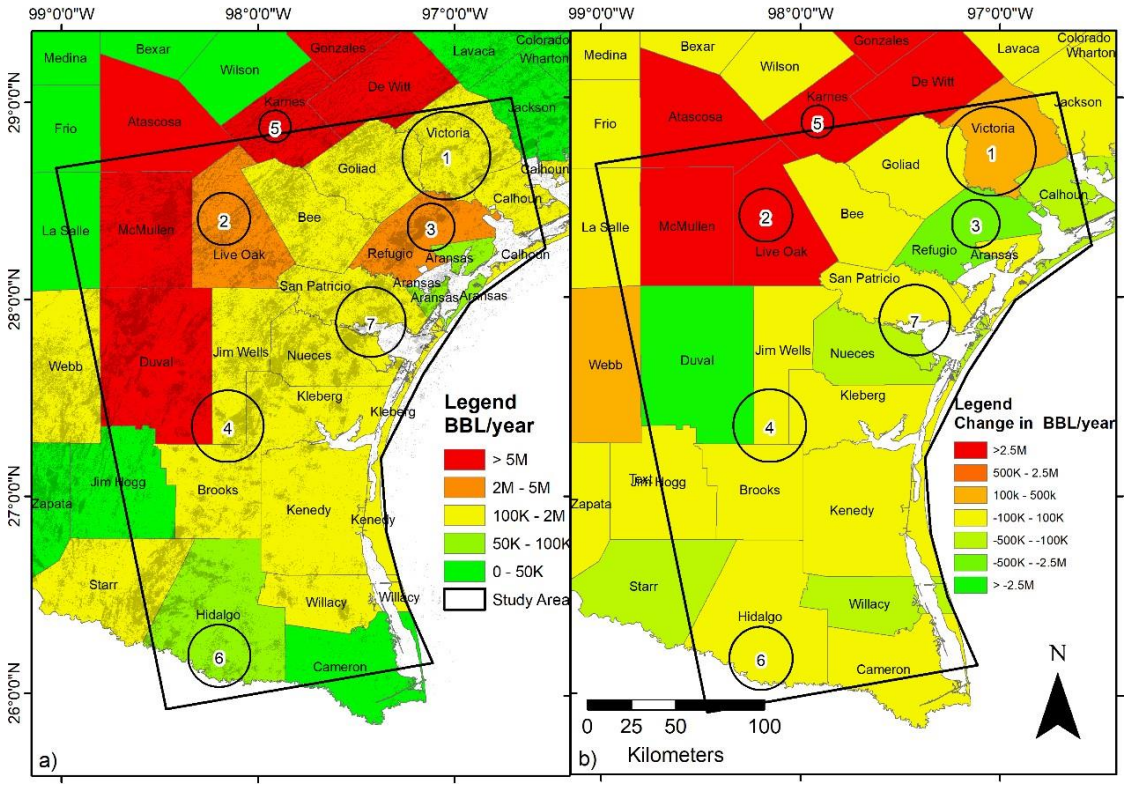

Figure 4: (a) Map showing historical oil/gas extraction (in BBL/yr) averaged by county during the period from 2000 to 2015. (b) Difference between groundwater extraction (in m^3/yr) between the study period (2016-2019) and the historical period (2000-2015). Circles 1 to 7 are areas that were identified to witness a significant land subsidence during the investigated period.

CHAPTER II

Data and Methods

1. Data

This was broken into three separate workflows. First, quantifying land subsidence rates and mapping land subsidence locations using radar images. Second, collecting relevant auxiliary datasets (e.g., fluid extraction rates, geologic structures) to investigate factors controlling the observed land deformation. Lastly, the generated land deformation rates were correlated with flooded areas extracted from radar images right after major flood events to examine if land subsidence made areas more susceptible to flooding. Two flood events were selected for this purpose, Hurricane Harvey (August 2017) and Hurricane Hanna (July 2020).

We used Synthetic Aperture Radar (SAR) data to map quantify land subsidence locations and rates within our study area. SAR data is provided by the Sentinel-1 mission (C-Band with a 5.56 cm wavelength) operated by the European Space Agency (ESA) under the Copernicus program. Sentinel -1 was launched in April 2014 to provide SAR imaging for all global landmasses and coastal zones with high spatial and temporal resolution (ESA 2012). A total of 68 Single Look Complex (SLC) Sentinel 1 scenes spanning the period from October 2016 to July2019 were used in this study. Sentinel-1 scenes were acquired in the Interferometric Wide (IW) imaging mode (scene width: 250 km) with spatial and temporal resolutions of 20 m and 12 days, respectively. These scenes were collected along track 107 frames 83 and 88 in the ascending direction (Table 1). Sentinel-1 data was downloaded from the Alaskan Satellite Facility. It is worth mentioning that it is preferable to combine both descending and ascending datasets to extract three-dimensional (3D) displacement rates. However, the descending direction does not provide adequate coverage of our study area. For flood mapping, we used the ascending track

107 frame 88 (Table 2) for the Harvey flood event. For Hanna we used descending track 41 frame 503 as it provided better temporal coverage of the storm event.

Table 1: Descriptions of the Sentinel-1 stacks used in this study.

Sar Instrument	Orbit Type	Track	Frame	No. of Images	Perpendicular Baseline		Temporal Baseline	
					Mean	Max	Mean	Max
Sentinel-1	Ascending	107	83	35	48	140	32	60
Sentinel-1	Ascending	107	88	33	45	147	24	60

Event	Sar Instrument	Orbit Type	Track	Frame	Pre-event images	Post Event Images
Harvey	Sentinel-1	Ascending	107	88	8	1
Hanna	Sentinel-1	Descending	41	503	2	1

Table 2. Descriptions of Sentinel-1 scenes used for flood mapping in this study.

To perform GPS-InSAR validation we downloaded GPS data from the Nevada Geodetic Laboratory through the GPS Networks Map (Blewitt et al. 2018). Data was extracted at 13 locations (Figure 1) throughout the study area during the same period as the SAR study (October 2016 – July 2019).

Growth Fault data was digitized from articles focusing on the Wilcox and Frio growth fault trends published by the Bureau of Economic Geology at the University of Texas at Austin (Ewing et al. 1987). Additionally, localized growth faulting in the Corpus Christi and NuecesBay area was digitized from an article focusing on the Lowstand Subbasin (Hammes et al. 2004)

(Figure 2). Oil and gas extraction rates were retrieved from the "Oil and Gas Production Data Query" which is maintained and updated by the Texas Railroad Commission (RRC; available here: https://www.rrc.state.tx.us/). We retrieved production data, by county between January 2000 – January 2020 (Figure 2). Groundwater extraction data was collected from the Texas Water Development (TWDB) Groundwater Database Reports website (available here: https://www.twdb.texas.gov). We retrieved groundwater extraction data by county between 2000 – 2020 (Figure 3).

A continuous distribution of sand percent of the GCA was constructed from point measurements taken at geophysical log locations. Only logs with 70% coverage across the entire thickness were used in the calculations (Young et al. 2010).The sand percentage for eachgeologic unit was calculated by summing the total sand amount across the thickness of the geologic unit and dividing by the amount of the thickness for which the lithology was characterized. These calculations were normalized to the lithology that was known for example ifthe unit was 100m thick, but lithology was only known for 85m and the sand thickness was 75m then the sand percentage would be 88% (100*75/85) and not 75% (100*75/100) (Young et al. 2012).

2. Methods

a. Mapping Land Subsidence Rates and Locations:

Persistent Scatterer (PS) technique was used in this study to quantify land subsidence rates. The PS uses a series of radar images to detect coherent PS points in the region of interest.A persistent scatter is a pixel that remains stable throughout the entire time period of the SAR acquisition. A primary image is chosen from the group of images based on favorable geometry, high coherence, and minimal atmospheric interference. Generally, urban areas are best suited for this because many fixed reflectors (e.g., buildings and utility poles) are available there. After the

primary and secondary images have been coregistered, interferograms are created. The main goal of PS is to decipher the coherent radar signals from incoherent noise by using the PS points as a reference (Hooper and Zebker 2007; Hooper et al. 2007; Hooper 2008). The criterion to select stable pixels for PSI analysis is amplitude dispersion, which is the variations in amplitude within the different images. Pixels with low variance have a high coherence value and are selected as persistent scatterer candidates(Esmaeili and Motagh 2016).

This study has been completed using the open-source software packages provided by ESA, the SentiNel Application Platform (SNAP) (Foumelis et al. 2018) and by the Stanford Method for Persistent Scatterers StaMPS (Hooper et al. 2007). Figure 5a shows a flow diagram of this process and Appendix 1 lists detailed steps for both SNAP and StaMPS processing(Höser 2018).

The PS Processing is conducted in two separate workflows, single master Differential Interferometric Synthetic Aperture Radar (DInSAR) processing using SNAP, and PS analysis using StaMPS. The master scene was selected using the "stack overview" routine in SNAP. This routine selects an optimal master scene for the stack based on the image which maximizes the coherence in the interferometric stack. The master image is then split into a subswath using the "S-1 tops split" function to make it compatible as a "snap2stamps' input. In this study this step was repeated for 5 separate subswaths. We used IW1, IW2, and IW3 in Frame 88 and only IW1 and IW2 in frame 83 to completely cover our study area (Table 1).

The next step creates the single master interferograms using the snap2stamps workflow to automatically create the single master interferograms. This package provides a set of python scripts that call routines from SNAP and perform automatic interferogram stacking that iscompatible with StaMPS PS analysis (Blasco and Foumelis 2018). Snap2stamps is implemented by running the four following scripts (Figure 5a): (1) Slave preparation: This script takes the

available Sentinel data within the project folder and separates it into individual folders by acquisition date. (2) Slave splitting: This step splits the slave images into the correct AOI and applies orbital corrections through SNAP.

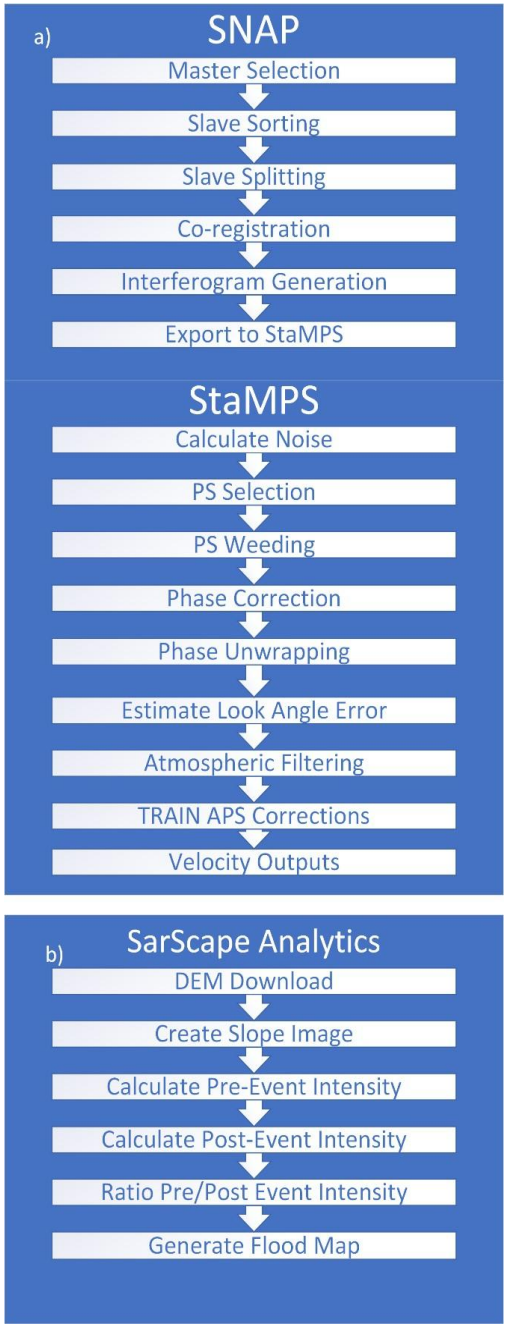

Figure 5: (a) SNAP and StaMPS workflows used to generate land deformation rates. (1) SarScape Analytics workflow used for flood mapping.

(3) Co-registration and interferogram generation: This step performs a co-registration of the SAR data and produces a set of interferograms with topographic phase removed. The outputs from this step are two stacks of master-slave SLC files and the master-slave interferogram. This step also prepares separate files that are required for the execution of StaMPS analysis. (4) StaMPS export: The final step that converts the interferograms into binary files that are compatible as StaMPS inputs. After the interferograms are in binary form the "mt_prep_snap" command is run to ingest the SNAP products into the StaMPS environment. We then ran the StaMPS process chain from steps 1-7 as described in the StaMPS User Manual (Hooper et al. 2010) to generate land subsidence rates (Figure 6). For the removal of the Atmospheric Phase Screen (APS), we have employed the Toolbox for Reducing Atmospheric InSAR Noise (TRAIN) and applied the Generic Atmospheric Correction Online Service for InSAR (GACOS) method for corrections(Yu et al. 2017, 2018a, b). APS corrections implements a weather model to predict realistic and real time atmospheric conditions and help overcome some limitations of SAR imaging such as cloud coverage and interference in the APS (Jung et al. 2014). If weather corrections are not applied, it is possible to be left with false deformation results as APS has effects on the observed topography in the image.

The adopted PS method generates multiple three-pass interferograms; however, it restricts the phase unwrapping and analysis to pixels containing individual scatterers that dominate individual pixels and remain stable over the time period of interest. Because the signal from these scatterers is much larger than the random noise from a large number of smallscatterers, the phase variance in these pixels reflects the underlying deformation (Crosetto et al. 2016).

b. InSAR-GPS Validation

Linear vertical velocities were estimated at the 13 GPS locations using daily position data spanning the period from October 2016 to July 2019. These GPS-derived velocities were then compared to InSAR-derived velocities. We assumed the InSAR Line of Sight (LOS) velocities were mostly vertical and used the average velocity of points within a 500 m radius of the GPS stations (Figure 6c). Uncertainty in GPS- and InSAR-derived velocities were calculated asfollows: (1) horizontal error bars (x-axis; InSAR) is represented by the standard deviation of all measurements located within a circle of a 500 m radius that is centered at the location of the GPSstation; (2) vertical error bars (y-axis; GPS) is represented by the standard deviation of daily GPSmeasurements at that station.

c. Mapping Flooded Areas

Senitinel-1 images were used for change detection flood mapping based on multi- temporal SAR images. This method relies on using multiple pre-event reference images that do not exhibit flooding in contrast to a post event image that has inundated areas. The coherence changes between the different images can then be classified as flooded or not flooded areas based on ratio between the flooded and reference images (Inglacla and Mercier 2007; Zhang et al. 2020) (Figure 5b).We implemented this method using the SARscape Analytics packagewithin ENVI software. The "SAR Flood Mapping" routine was used, and adjustments were made using the SAR Flood Mapping Classification-Refinement (Bahr and Europe 2020). To map inundated areas after Hurricane Harvey we used 4 pre-event images as a control background for the unflooded study area. We then picked a post-event image that was as close as possible to the

major event. Using the SAR Flood mapping tool, we then picked inundated areas by selecting a ratio between pre and post event coherence to determine which areas have been flooded by the storm event.

CHAPTER III

Results

1. Land Subsidence Rates and Locations

Examination of Figure 6a reveals that land deformation in the study area is spatially heterogenous with localized areas of subsidence as high as -21 mm/yr. Additionally, some localized areas show a land uplift with rate of > 10 mm/yr. Figure 6b shows a histogram for land deformation rates over the Texas Coastal Bend region. Inspection of this histogram indicates that the average deformation rate is estimated at -1.27 ±3.2 mm/ar.

The InSAR-derived ground deformation rates were compared to those extracted from 13 GPS stations located within the study area. Figure 6c shows a scatterplot of InSAR-derived versus GPS-derived ground deformation rates along with a 1:1 line. Examination of Figure 6c shows that the GPS-derived ground deformation rates were consistent with deformation rates obtained from InSAR analysis. The mean difference between GPS and InSAR-derived velocities at all 13 stations is estimated at 2.23 mm/yr ±2.7 mm/yr.

Seven regions were observed to experience significant land subsidence rates along Texas Costal bend region during the investigated period. These regions are, Victoria, George West, Refugio, Falfurrias, Karnes City, McAllen, and Nueces Bay/CorpusChristi (polygons 1-7; Figure 6a). We Believe land subsidence in these regions is attributed mainly to fluid extraction as well as vertical movements along growth faults.

Fluid extraction is an important controlling factor in land subsidence due to compaction of sediments in response to the withdrawal of fluid. When fluid is extracted from underlying strata it reduces the pore pressure within the layer, and in turn increases the effective stress on

the grains themselves. The increased effective stress on the grains can cause the layer to compact and thus the subsidence of overlying land surface. Clay rich sediments are much more prone to compaction since they often have much higher porosity values, and thus the decrease in pore pressure leaves more void space.

Lithology is also a known controlling factor in land subsidence as mentioned earlier, clay rich sediments are subject to compaction under increased effective stress. We mapped the sand percentage of the study area (Figure 2c) and found some spatial variation within the study area. Sand percentage for the majority of the polygons with the exception of polygons 2 and 4 is within 50% - 70%. Because it is homogeneous in these polygons, we do not consider the lithology to be a controlling factor of subsidence in these regions. While Polygon 2 sees a higher average sand percent (60% - 80%) we do not believe this to have an effect on increased subsidence as an increase in sand percentage we do not believe this to be a controlling factor due to subsidence being characterized with higher clay percentages. Polygon 4 sees a much lower sand percentage that the other polygons (30% - 50%) and we do believe this to possibly have an effect on the increased subsidence in this region.

Growth faults in coastal areas are known to cause subsidence (Campbell et al. 2015) due to their nature of being normal faults with the hanging wall being on the coastal side of the fault plane. Our study area is littered with growth faults (figure 2a) as it is located on a passive coastal margin. We mapped fault density (Figure 2b) to show a relationship between the amount of faulting in a given area and subsidence rates. Additionally, there is strong evidence that the extractions of fluids from subsurface sediments can accelerate or reinitiate movement along these faults ((Verbeek and Clanton 1981).

For the purpose of this study, we classified oil/gas extraction rates to low in Barrels (BBL) (100 $\times 10^3$ BBL), medium (100 $\times 10^3$ – 2 $\times 10^6$ BBL), and high (> 2 $\times 10^6$ BBL).

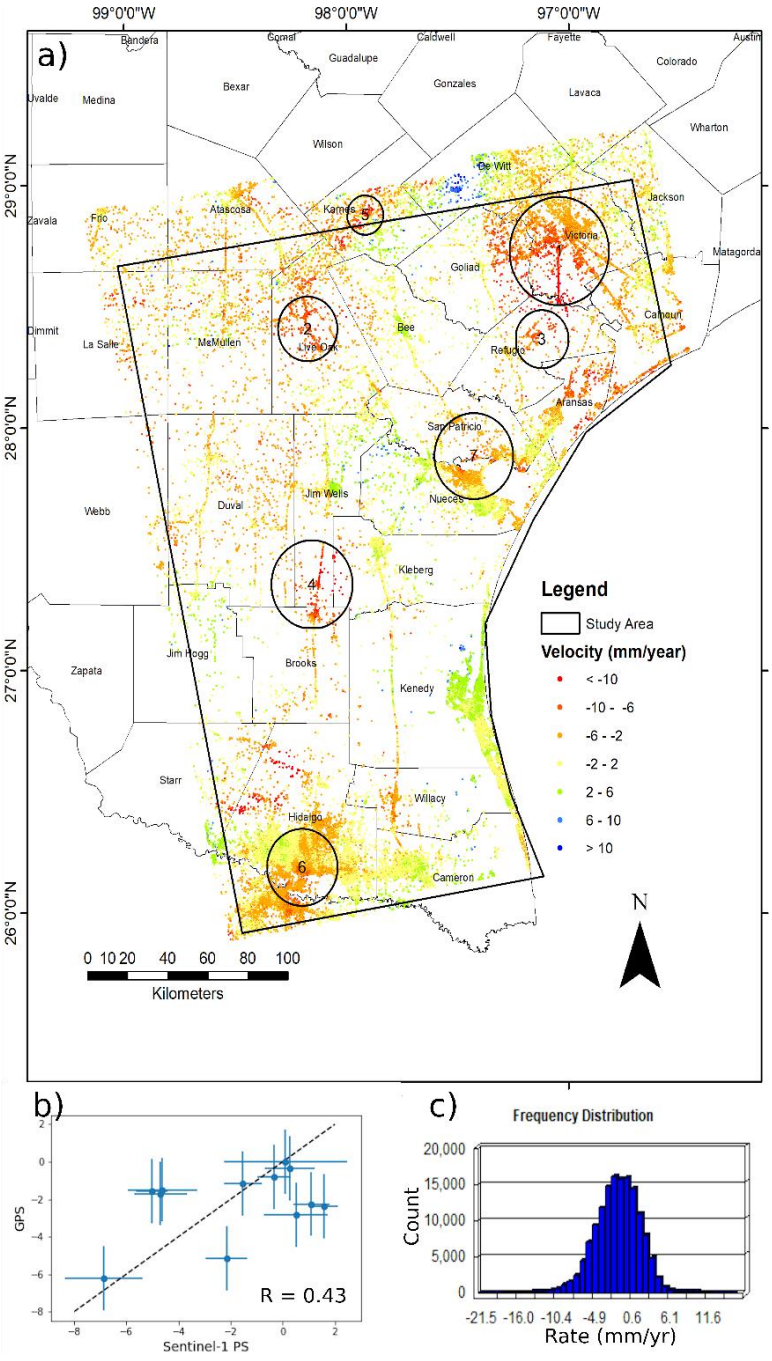

Figure 6: (a) land subsidence rates (in mm/yr) generated over the Texas Coastal Bend during the period from 2016 to 2019. (b) Correlation of InSAR-derived land deformation rates (in mm/yr) with GPS-derived land deformation rates. (c) Histogram of land subsidence rates.

Groundwater extraction rates were classified into low (< 2×10^6 m^3), medium (2×10^6 m^3–7.5×10^6 m^3), and high (7.5×10^6 m^3). Finally, growth fault density was classified into low (0-10 km/km^2), medium (10-15 km/km^2), and high (>15 km/km^2). Below, we explain factors controlling the observed land subsidence rates in each of these regions.

2. Factors Controlling Observed Land Subsidence Rates

The highest subsidence rates were observed in the city of Victoria with rates of -5.3 ±2 mm/yr (polygon 1; Figure 6a). Localized subsidence rates as high as -11.6 ± 3.0 mm/yr were also observed south of Victoria. Increased subsidence rates could be attributed to enhanced oil/gas and groundwater extraction activities during the study period, high historic extraction rates, as well as vertical movements along growth faults. This assumption is supported by the observed increase in oil/gas extraction rates (431×10^3BBL/yr; Figure 4b) during the investigated period compared to the long-term average annual extraction rates (groundwater: 18×10^6 m^3/yr; oil/gas: 664×10^3 BBL/yr; Figure 3a, 4a). In addition, this area has a high fault density: > 0.15 km/km^2; (Figure 2b) that could also accelerate the subsidence rates.

Live Oak County near the town of George West is also witnessing land subsidence with rates of -7.6 ± 1.7 mm/yr (polygon 2, Figure 6a). We believe the subsidence in this area could be attributed to a combination of both growth faulting and enhanced oil/gas extraction during the study period. Live Oak County reported a very large increase of oil/gas extraction (7.65×10^6 BBL/yr; Figure 4b) compared to its historical rate (2.98×10^6 BBL/yr; Figure 4a) while there was a slight decrease in groundwater extraction (-78.2×10^3 m^3/yr; figure 3b) compared to the

historical average of (5.2×10^6 m^3/yr; figure 3a). Additionally, there is a high density of growth faults being observed in the area surrounding George West (> 0.15 km/km^2, Figure 2b).

The town of Refugio witnesses land subsidence with average rates of -6.8±1.6 mm/yr (polygon 3, Figure 6a). Refugio County has a medium to high degree of fault density (0.1- 0.25) (Figure 2b) that overlaps the area of increased subsidence which we believe to be the main controlling factor for the observed subsidence in this area because the extraction rates for both oil/gas (-1.25 × 10^6 BBL/yr; Figure 4b) and groundwater (-251 × 10^3 m^3/yr Figure 3b) have decreased compared to their respective historic annual averages (oil/gas: 3.84 × 10^6 BBL/yr: Figure 4a; groundwater:2.84 × 10^6 m^3/yr: Figure 3a).

The city of Falfurrias in Jim Wells County (polygon 4, Figure 6a) experienced a land subsidence at rate of -8.0±2.6 mm/yr. We believe this area is primarily controlled by growth faulting and lithology as the extraction rates in the area of both oil/gas and groundwater have remained very similar to the historical averages (oil/gas: 138 × 10^3 BBL/yr: Figure 4a; groundwater: 6.05 × 10^6 m^3/yr; Figure 3a). Although this area is witnessing a low to medium amount of fault density (0-0.15; Figure 2b), two prominent growth faults sandwich the subsided region, potentially explaining the observed subsidence. Additionally, Polygon 4 shows a much lower sand percentage compared to the other regions focused on in this study. We believe that the lower sand percentage and resulting higher clays percentage could be contributing to the increase in observed subsidence.

Karnes City witnessed an averaged land subsidence rate of -6.7±3.9 mm/yr (polygon 5, Figure 6a). Fluid extraction is the primary controlling factor in the subsidence, as Karnes County reported a large increase in both oil/gas (78.04 × 10^6 BBL/yr; Figure 4b) and groundwater (9.29 × 10^6 m^3/yr; Figure 3b) extraction rates during the study period as compared to the historical

rates (oil/gas:18.23 × 10^6 BBL/yr; Figure 4a; 6.85 × 10^6 m^3/yr; Figure 3a) respectively. Fault density in the area is 0 km/km^2 (Figure 2b) so growth faults were not believed to be a controlling factor in this area.

In Hidalgo County land subsidence (-3.0±1.8 mm/yr) is centered around the McAllen metro area that includes the cities of Edinburgh and Mission. Localized areas within this region experienced land subsidence rates as high as -11±2.1 mm/yr (polygon 6, Figure 6a). Land subsidence in this area is believed to be due to both growth faulting and groundwater extraction. Hidalgo County reported an increase in groundwater extraction of 5.27 × 10^6 m^3/yr during the study period in conjunction with the high historical average annual rate (14.62 × 10^6 m^3/yr; Figure 3a). Hidalgo County has a low fault density value (< 0.1 km/km^2). Hidalgo has witnessed a very minor decrease in oil and gas extraction during the study period (-6.30 × 10^3 BBL/yr), and also historically has a low amount of oil extraction (59.39 × 10^3 BBL/yr).

Nueces Bay area, especially in the port corridor, experiencing a land subsidence with rates of -3.4±1.6 mm/yr (polygon 7, Figure 6a). This is believed to be due to the presence of growth faulting in the area (fault density: >0.15 km/km^2; Figure 2b) that affect in both Corpus Christi and Nueces Bays. We do not think fluid extraction is a factor contributing to subsidence here as Nueces and San Patrictio Counties have witnessed a decrease in oil/gas extraction rates (-62.5 × 10^3 BBL/yr in San Patricio County; -262.5 × 10^3 BBL/yr in Nueces County; Figure 4b). San Patricio County has even experienced a large decrease in groundwater extraction (-4.5 × 10^6 m^3/yr Figure 3b) as compared to historical rates of (13.3 × 10^6 m^3/yr; figure 3a).

3. Consequences of Land Subsidence in Coastal Texas

The InSAR-derived deformation rates have been spatially correlated with the spatial distribution of areas affected by recent flood events in the Coastal Bend (Figure 7). We decided to examine areas that were shortly inundated after Hurricane Harvey in August 2017 and Hurricane Hanna in July 2020. These two storms heavily impacted the South Texas coast with heavy rainfall (Emanuel 2017; Brown et al. 2020). Figure 7a shows the rainfall amounts at stations for each storm event. Hurricane Harvey showed rainfall totals ranging between 93mm in Orange Grove to as high as 330 mm in Refugio. Hurricane Hanna saw rates between 165 mm in Weslaco to as high as 311 mm north of McAllen. The main goal is to investigate if there was a connection between the observed subsidence rates and flooding aftermath of storm events within our study area.

We focused on two main area, the Hidalgo county (polygon 6, Figure 7) and the Nueces Bay (polygon 7, Figure 7). These two areas were selected for two reasons: (1) they are most affected by flooding events (Figure 7), and (2) they contain the two largest population centers within the Coastal Bend, McAllen (polygon 6) and Corpus Christi (polygon 7).

Our results indicated that Hurricane Hanna flooded a total area of 2,225 km^2, while hurricane Harvey flooded area was estimated at 1,020 km^2. We believe that we observe much more flooding in the after math of Hanna due to the temporal baseline between the storm event and the post event image differences, with the Harvey flooding being largely underestimated.

It appears that most of the areas that remained inundated in the post event images consisted of cultivated cropland (Figure 7b). We believe this to be because coherence-based flood mapping is more effective in rural areas. This is explained by even with water having a low backscatter response, the structures within urban areas will provide bright pixels that dominate the area,

while in rural areas such as farmland there will be a significant drop in coherence due to the presence of water. Additionally, urban areas have better drainage solutions, so they will not remain inundated for as long after a storm event.

We compared the average subsidence rates of the non-flooded areas to the average subsidence rates of the flooded areas in each polygon. We observed that subsidence rates within flooded areas are significantly higher than that of the non-flooded areas. For example, the average subsidence rate of the non-flooded area in polygon 6 is -2.20 ± 2.30 mm/yr, while the average subsidence rate of the areas flooded in the aftermath of Hanna within polygon 6 are -2.71 ± 2.15 mm/yr. The same applies to polygon 7. In polygon 7, the average subsidence rate of the non-flooded areas is estimated at -2.76 ± 1.83 mm/yr which is only 68% of the average subsidence rate (-4.04±1.89 mm/yr) of the areas flooded in the aftermath of Harvey within polygon 7.

We examined the statistical significance of the difference in subsidence rates been flooded and non-flooded area. The Welch's two-sample t-test (Welch 1938)) was used to test if there is indeed a significant difference between the in the mean subsidence rates in flooded and non-flooded areas in polygons 6 and 7. For polygon 6 our results show that the inundated areas in the aftermath of hurricane Hanna show a significantly higher rate of subsidence than the non-flooded areas ($t = 6.72$, $p = 3.14e^{-11}$). Similarly, for polygon 7 the areas flooded during hurricane Harvey witnessed a significantly higher rate of subsidence compared to the non-flooded areas ($t = 7.19$, $p = 5.29e^{-16}$). The increased subsidence in these areas is believed to a contributing factor to the areas becoming inundated during heavy rainfall events.

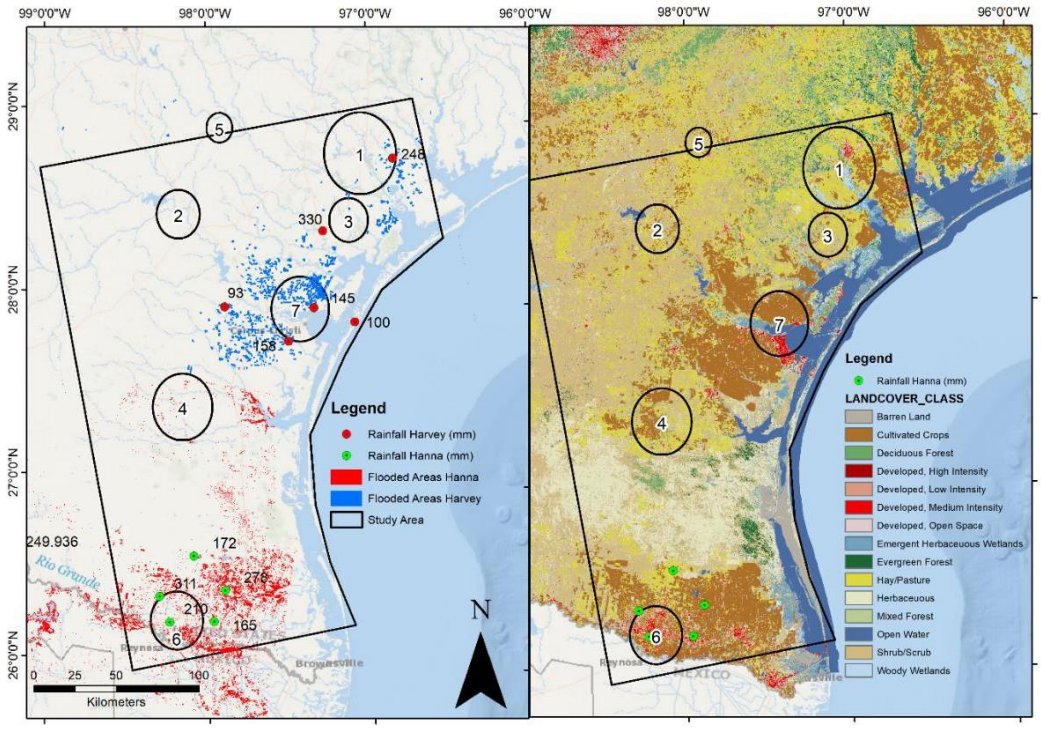

Figure 7: (a) Map showing areas inundated after hurricane Harvey (blue polygons), and Hurricane Hanna (red polygons). Rain amounts in millimeters are also listed for Hanna (green circles) and Harvey (red circles) as reported by NOAA (b) Map showing land cover types within the study area.

While we see a significant connection between flooded and subsided areas within polygon 6 and polygon 7, some regions within the Coastal Bend witnessed a land subsidence but not flooded (e.g., polygons 1, 3, and 4). This could be attributed to the fact that the Coastal Bend is very diverse in the spatial domain and additional factors could exert controls on areas that are being flooded in the aftermath of heavy rainfall. Other regions (polygons 2 and 5) were away from the storm path. We also see flooding in areas that are not witnessing severe subsidence in our study area , and while we believe that subsidence is a key component in causing

susceptibility to floods, we also recognize that it is possible for these areas to experienceflooding due to other major factors that affect flood susceptibility such as the actual elevation of the flood plains, topography, vegetation, the path of the storm, spatial variability in rainfall intensity, and hydrologic conditions preceding the storm event.

Subsided areas along the Texas Coastal Bend are believed to witness not only frequent, but also severe flood events. Land subsidence rates and sediment compressibility are linearly related (Teatini et al. 2011). Sediment compressibility directly affects flooding severity. For example, highly compressible deltaic sediments were reported to erode, break up, and become submerged more rapidly compared to other types of sediments (Bourman et al. 2000). Such compressible layers experience consolidation with changes in the vertical load (Harris et al. 2020). Consolidation rapidly reduces elevation and thereby increases the susceptibility to severe inundation following a flooding or storm event.

CHAPTER IV

Discussion and Conclusion

1. Discussion

This research integrates different remote sensing data and techniques to develop enhanced land subsidence datasets in the Coastal Bend area of Texas. This study developed an improved understanding of spatial correlations between natural (e.g., growth faults) and anthropogenic (e.g., fluid extraction) processes that could be controlling coastal subsidence. Our study shows significant correlations between growth faulting and fluid extraction with land subsidence in coastal areas. This is congruent with previous InSAR studies that have been conducted in the Houston area as well as in other parts of the United States where these two factors also show correlations with observed subsidence rates. Our results will enhance the prediction of Coastal Bend communities' responses to natural forces rise and will eventually facilitate extreme-event mitigation and remediation. This, in turn, will improve the resiliency of Texas coastal communities. Decision makers could use these results to explore sustainable mitigation scenarios while preserving the unique nature of valuable coastal resources.

This study has some limitations, primarily in the temporal coverage of the radar scenes used to map land subsidence rates and locations as well as flood mapping. Our study period is quite short, however other satellite platforms (e.g., ENVISAT, PALSAR) make it possible to extend this range to cover the entire 21st century. We believe that the short study period could be an issue in the sense that subsidence is a long-term problem, and we have only captured a snapshot of this with a 4-year study period. This means that the rates presented in this study; while accurate, may not be representative of the historical land subsidence rates.

Another limitation of this study is the lack of bidirectional coverage from sentinel scenes within out area. There are only ascending scenes available within our study area which provide

adequate coverage. Due to this limitation, we are not able to calculate true vertical deformation from our LOS velocities, we can only assume that the movement of the PS is purely vertical. LOS velocities are the product of movement in three spatial axes (North. East, Vertical) , although primarily in the vertical direction. If two acquisition directions are available. it possible to use trigonometry in conjunction with incidence angle of each pixel to subtract the north and east movement vectors and be left with the true vertical displacement that does not include the slight movements in the other two directions.

We faced some challenges in the flood mapping exercise, mainly the lack of ground truthing data and temporal separation between the storm image and next available radar image in the Harvey storm event. There were no images available in the immediate hours or day after the storm events. In the case of Harvey, the first available image for flooding is 7 days post landfall of the storm on September 3, 2017. Because of this, it is likely that the areas that are shown as inundated do not show the full extent of flooding that actually occurred within the study area. We believe that due to the temporal difference in acquisition dates that our map is heavily underestimating the amount of flooding in Hurricane Harvey, especially in the areas near the coast where flood waters would dissipate quickly.

Additionally, high resolution optical images from NOAA only exist in the Rockport area for hurricane Harvey, while no imagery is available in for Hanna. The optical images for Harvey were acquired on August 29, 2017, 4 days prior to the Post-event image that we have available. We believe that again, this temporal difference makes the use of this optical image as a validation method impossible. We also attempted using optical satellite images from Landsat and Sentinel 2 to verify the flood results; however, the images close in temporal baseline to the flood events were extremely cloudy and could not be used as validation.

Lastly, when comparing GPS measurements to InSAR measurements there are two limitations that could be leading to discrepancies in the comparisons. First, GPS rates are calculated from measurements that are taken daily, while InSAR measurements in this study have a temporal baseline of roughly 1 month (Table 1). Secondly, the SAR acquisitions as mentioned earlier are not in true vertical domain but assumed to be vertical due to the lack of bidirectional radar coverage within the study area.

2. Conclusion

The objectives of this study were to map land subsidence rates and locations in the Texas Coastal Bend between 2016 – 2019, investigate the factors controlling the observed subsidence rates, and explain the consequences of these subsidence. We identified rapid local land subsidence in the Coastal Bend regions such as Victoria, George West, McAllen, Karnes City, and Corpus Christi. We suggest that these rapid subsidence rates are the result of both natural and anthropogenic factors, namely the heavy growth faulting dissect the coastal plains of Texas along with high fluid (oil and groundwater) extraction rates seen in some counties. Additionally, we were able to map areas flooded in the aftermath of two recent tropical cyclones and compare the subsidence rates in flooded areas to those of the areas not affected by flooding in the two largest population centers in the study area. We found that there was a significant increase in the average subsidence rates within the flooded areas compared to those that were not flooded.

With the projected rise in sea levels coupled with both natural and anthropogenic induced subsidence, the Coastal Bend communities are facing an increased risk of flooding. The study area has already witnessed a significant number of tropical cyclones, however land subsidence in this region is working as an amplifying effect of what is already one of the most destructive forces on earth, the flood. Our results signal the need to generate a complementary longer land

deformation time series using InSAR platforms such as Envisat and Palsar to better understand the spatial and temporal variabilities in land subsidence locations and rates as well as factors controlling the observed subsidence rates. Additionally, these InSAR platforms could also be used to better map inundated areas, which could help in the mitigation of the effects of future flood events. This study serves as a warning that subsidence is an ongoing issue in south Texas and if not monitored closely could have huge detrimental effects for the region in the future.

REFERENCES

Abidin HZ, Andreas H, Gumilar I, et al (2013) Land subsidence in coastal city of Semarang (Indonesia): Characteristics, impacts and causes. Geomatics, Nat Hazards Risk 4:226–240. https://doi.org/10.1080/19475705.2012.692336

Aslan G, Lasserre C, Cakir Z, et al (2019) Shallow Creep Along the 1999 Izmit Earthquake Rupture (Turkey) From GPS and High Temporal Resolution Interferometric Synthetic Aperture Radar Data (2011–2017). J Geophys Res Solid Earth 124:2218–2236. https://doi.org/10.1029/2018JB017022

Bahr T, Europe SE (2020) Sarscape analytics toolbox

Baker ETJ (1995) Stratigraphic Nomenclature and Geologic Sections of the Gulf. US Geol Surv Open-File Rep 94–461:34

Bawden GW, Johnson MR, Kasmarek MC, et al (2012) Investigation of land subsidence in the Houston-Galveston region of Texas by using the Global Positioning System and interferometric synthetic aperture radar, 1993-2000

Blachowski J, Kopec A, Milczarek W, Owczarz K (2019) Evolution of secondary deformations captured by satellite radar interferometry: Case study of an abandoned coal basin in SW Poland. Sustain 11:. https://doi.org/10.3390/su11030884

Blackwell E, Shirzaei M, Ojha C, Werth S (2020) Tracking California's sinking coast from space: Implications for relative sea-level rise. Sci Adv 6:1–10. https://doi.org/10.1126/sciadv.aba4551

Blasco JMD, Foumelis M (2018) Automated SNAP Sentinel-1 DInSAR processing for StaMPS PSI with open source tools. Autom Sn Sentin DInSAR Process StaMPS PSI with open source tools. https://doi.org/10.5281/zenodo.1308687

Blewitt G, Hammond W, Kreemer C (2018) Harnessing the GPS Data Explosion for Interdisciplinary Science. Eos (Washington DC) 99:1–9. https://doi.org/10.1029/2018eo104623

Bourman RP, Murray-Wallace C V., Belperio AP, Harvey N (2000) Rapid coastal geomorphic change in the River Murray Estuary of Australia. In: Marine Geology. Elsevier, pp 141–168

Brown DP, Berge R, Brad R (2020) National Hurricane Center Tropical Cyclone Report. Hurricane Hanna. 1–49

Bruun B, Jackson K, Lake P, Walker J (2016) Texas Aquifers Study Groundwater Quantity, Quality, Flow, and Contributions to Surface Water

Campbell MD, Campbell DM, Wise HM, Bost RC (2015) Growth Faulting and Subsidence in the Houston, Texas Area: A Guide to the Origins, Relationships, Hazards, Potential Impacts, and Methods of Investigation. 102. https://doi.org/10.13140/RG.2.1.4396.5604

Chowdhury AH, Ph D, Mace RE, Ph D (2001) Chapter 10 Groundwater Models of the Gulf Coast Aquifer of Texas. 173–204

Chowdhury AH, Wade S, Mace RE, Ridgeway C (2004) Groundwater Availability Model of the Central Gulf Coast Aquifer System: Numerical Simulations through 1999. 114

Dolan AH, Walker IJ (2006) Understanding Vulnerability of Coastal Communities to Climate Change Related Risks. J Coast Res III:1316–1323

Don NC, Hang NTM, Araki H, et al (2006) Salinization processes in an alluvial coastal lowland plain and effect of sea water level rise. Environ Geol 49:743–751. https://doi.org/10.1007/s00254-005-0119-7

Dzurisin D, Lu Z (2006) Interferometric synthetic-aperture radar (InSAR)

Eggleston J, Pope J (2013) Land Subsidence and Relative Sea-Level Rise in the Southern

Chesapeake Bay Region

Emanuel K (2017) Assessing the present and future probability of Hurricane Harvey's rainfall. Proc Natl Acad Sci U S A 114:12681–12684. https://doi.org/10.1073/pnas.1716222114

ESA (2012) ESA's radar observatory mission for GMES operational services

Esmaeili M, Motagh M (2016) Improved Persistent Scatterer analysis using Amplitude Dispersion Index optimization of dual polarimetry data. ISPRS J Photogramm Remote Sens 117:108–114. https://doi.org/10.1016/j.isprsjprs.2016.03.018

Ewing TE, Anderson R., Babalola O, et al (1987) Structural Syles of the Wilcox and Frio Growth-Fault Trends in Texas: Constraints on Geopressured Resevoirs.

Felsenstein D, Lichter M (2014) Social and economic vulnerability of coastal communities to sea-level rise and extreme flooding. Nat Hazards 71:463–491. https://doi.org/10.1007/s11069-013-0929-y

Ferretti A, Fumagalli A, Novali F, et al (2011) A new algorithm for processing interferometric data-stacks: SqueeSAR. IEEE Trans Geosci Remote Sens 49:3460–3470. https://doi.org/10.1109/TGRS.2011.2124465

Fiaschi S, Wdowinski S (2020) Local land subsidence in Miami Beach (FL) and Norfolk (VA) and its contribution to flooding hazard in coastal communities along the U.S. Atlantic coast. Ocean Coast Manag 187:105078. https://doi.org/10.1016/j.ocecoaman.2019.105078

Fitzgerald DM, Fenster MS, Argow BA, Buynevich I V (2008) Coastal Impacts Due to Sea-Level Rise. Annu Rev Warth Planet Sci 36:601–647. https://doi.org/10.1146/annurev.earth.35.031306.140139

Foumelis M, Blasco JMD, Desnos YL, et al (2018) ESA SNAP - Stamps integrated processing for Sentinel-1 persistent scatterer interferometry. Int Geosci Remote Sens Symp 2018-

July:1364–1367. https://doi.org/10.1109/IGARSS.2018.8519545

Galloway DL, Burbey TJ (2011) Review: Regional land subsidence accompanying groundwater extraction. Hydrogeol J 19:1459–1486. https://doi.org/10.1007/s10040-011-0775-5

Galloway DL, Hudnut KW, Ingebritsen SE, et al (1998) Detection of aquifer system compaction and land subsidence using interferometric synthetic aperture radar, Antelope Valley, Mojave Desert, California. Water Resour Res 34:2573–2585. https://doi.org/10.1029/98WR01285

Gebremichael E, Sultan M, Becker R, et al (2018) Assessing Land Deformation and Sea Encroachment in the Nile Delta: A Radar Interferometric and Inundation Modeling Approach. J Geophys Res Solid Earth 123:3208–3224. https://doi.org/10.1002/2017JB015084

Grineski SE, Flores AB, Collins TW, Chakraborty J (2019) The impact of Hurricane Harvey on Greater Houston households: Comparing pre-event preparedness with post-event health effects, event exposures, and recovery. Disasters. https://doi.org/10.1111/disa.12368

Hammes, Loucks U, Brown R., et al (2004) Structural Setting and Sequence Architecture of a Growth-Faulted. Corpus 54:237–246

Harris BD, Johnson C, Jafari NH, et al (2020) Effects of coupled consolidation and overwash processes on a low-lying headland system. Coast Eng 160:103746. https://doi.org/10.1016/j.coastaleng.2020.103746

Hooper A, Segall P, Zebker H (2007) Persistent scatterer interferometric synthetic aperture radar for crustal deformation analysis, with application to Volcán Alcedo, Galápagos. J Geophys Res Solid Earth 112:1–21. https://doi.org/10.1029/2006JB004763

Hooper A, Spaans K, Bekaert D, et al (2010) StaMPS / MTI Manual

Höser T (2018) SNAP - StaMPS Workflow - 1.1

Hu X, Bürgmann R, Lu Z, et al (2019) Mobility, Thickness, and Hydraulic Diffusivity of the Slow-Moving Monroe Landslide in California Revealed by L-Band Satellite Radar Interferometry. J Geophys Res Solid Earth 124:7504–7518. https://doi.org/10.1029/2019jb017560

Inglacla J, Mercier G (2007) A new statistical similarity measure for change detection in multitemporal SAR images and its extension to multiscale change analysis. IEEE Trans Geosci Remote Sens 45:1432–1445. https://doi.org/10.1109/TGRS.2007.893568

Jackson MPA, Roberts DG, Snelson S (2020) Cenozoic Structural Evolution and Tectono-Stratigraphic Framework of the Northern Gulf Coast Continental Margin. Salt Tectonics 109–151. https://doi.org/10.1306/m65604c6

Jung J, Kim DJ, Park SE (2014) Correction of atmospheric phase screen in time series InSAR using WRF model for monitoring volcanic activities. IEEE Trans Geosci Remote Sens 52:2678–2689. https://doi.org/10.1109/TGRS.2013.2264532

Khan SD, Huang Z, Karacay A (2014) Study of ground subsidence in northwest Harris county using GPS, LiDAR, and InSAR techniques. Nat Hazards 73:1143–1173. https://doi.org/10.1007/s11069-014-1067-x

Kim JW, Lu Z (2018) Association between localized geohazards in West Texas and human activities, recognized by Sentinel-1A/B satellite radar imagery. Sci Rep 8:1–13. https://doi.org/10.1038/s41598-018-23143-6

Massonnet D, Feigl KL (1998) Radar interferometry and its application to changes in the Earth's surface. Rev Geophys 36:441. https://doi.org/10.1029/97RG03139

Miller MM, Shirzaei M (2019) Land subsidence in Houston correlated with flooding from

Hurricane Harvey. Remote Sens Environ 225:368–378. https://doi.org/10.1016/J.RSE.2019.03.022

Miller MM, Shirzaei M, Argus D (2017) Aquifer Mechanical Properties and Decelerated Compaction in Tucson, Arizona. J Geophys Res Solid Earth 122:8402–8416. https://doi.org/10.1002/2017JB014531

Othman A, Sultan M, Becker R, et al (2018) Use of Geophysical and Remote Sensing Data for Assessment of Aquifer Depletion and Related Land Deformation. Surv Geophys 39:543–566. https://doi.org/10.1007/s10712-017-9458-7

Paine JG (1993) Subsidence of the Texas coast: inferences from historical and late Pleistocene sea levels. Tectonophysics 222:445–458. https://doi.org/10.1016/0040-1951(93)90363-O

Qu F, Lu Z, Zhang Q, et al (2015a) Mapping ground deformation over Houston–Galveston, Texas using multi-temporal InSAR. Remote Sens Environ 169:290–306. https://doi.org/10.1016/J.RSE.2015.08.027

Qu F, Lu Z, Zhang Q, et al (2015b) Mapping ground deformation over Houston-Galveston, Texas using multi-temporal InSAR. Remote Sens Environ 169:290–306. https://doi.org/10.1016/j.rse.2015.08.027

Qu F, Lu Z, Zhang Q, et al (2015c) Mapping ground deformation over Houston-Galveston, Texas using multi-temporal InSAR. Remote Sens Environ 169:290–306. https://doi.org/10.1016/j.rse.2015.08.027

Ryder PD, Ardis AF (2002) Hydrology of the Texas Gulf coast aquifer systems. US Geol Surv Prof Pap. https://doi.org/10.3133/pp1416E

Shan XJ, Ye H (1998) The INSAR technique: Its principle and applications to mapping the deformation field of earthquakes. Acta Seismol Sin English Ed 11:759–769.

https://doi.org/10.1007/s11589-998-0012-z

Small C, Nicholls RJ (2003) A global analysis of human settlement in coastal zones. J Coast Res 19:584–599

Stukey, Jared et. al (2004) Bay , and Sabine Lake Lower-Watershed Multi-year Land-Use and Land Cover Classifications and Curve Numbers TWDB Contract # 0804830788 by Spatial Sciences Lab , Department of Ecosystem Science and Management , and Texas A & M University

Teatini P, Tosi L, Strozzi T (2011) Quantitative evidence that compaction of Holocene sediments drives the present land subsidence of the Po Delta, Italy. J Geophys Res Solid Earth 116:8407. https://doi.org/10.1029/2010JB008122

Venkataramanan V, Packman AI, Peters DR, et al (2019) A systematic review of the human health and social well-being outcomes of green infrastructure for stormwater and flood management. J. Environ. Manage. 246:868–880

Verbeek ER, Clanton US (1981) Historically Active Faults in the Houston Metropolitan Area, Texas. Houst Geol Soc Houston Ar:28–68

Welch BL (1938) The Significance of the Difference Between Two Means when the Population Variances are Unequal. Biometrika 29:350. https://doi.org/10.2307/2332010

Wu SY, Yarnal B, Fisher A (2002) Vulnerability of coastal communities to sea-level rise: A case study of Cape May County, New Jersey, USA. Clim Res 22:255–270. https://doi.org/10.3354/cr022255

Young SC, Ewing T, Hamlin S, et al (2012) Final Report Updating the Hydrogeologic Framework for the Northern Portion of the Gulf Coast Aquifer. 283

Young SC, Knox PR, Baker E, et al (2010) Final Hydrostratigraphy of the Gulf Coast Aquifer

from the Brazos River to the Rio Grande. 1–213

Yu C, Li Z, Penna NT (2018a) Interferometric synthetic aperture radar atmospheric correction using a GPS-based iterative tropospheric decomposition model. Remote Sens Environ 204:109–121. https://doi.org/10.1016/j.rse.2017.10.038

Yu C, Li Z, Penna NT, Crippa P (2018b) Generic Atmospheric Correction Model for Interferometric Synthetic Aperture Radar Observations. J Geophys Res Solid Earth 123:9202–9222. https://doi.org/10.1029/2017JB015305

Yu C, Penna NT, Li Z (2017) Generation of real-time mode high-resolution water vapor fields from GPS observations. J Geophys Res 122:2008–2025. https://doi.org/10.1002/2016JD025753

Zhang M, Chen F, Liang D, et al (2020) Use of sentinel-1 grd sar images to delineate flood extent in Pakistan. Sustain 12:1–19. https://doi.org/10.3390/su12145784

Zilkoski DB, Hall LW, Mitchell GJ, et al (2003) The Harris-Galveston Coastal Subsidence District/National Geodetic Survey automated Global Positioning System subsidence monitoring Project. Proc US Geol Surv Subsid Interes Gr Conf 13–28

LIST OF APPENDICES

APPENDIX PAGE

Appendix 1
SNAP-StaMPS Detailed Tutorial

Installation and Configuration

1. Linux System
   Install a Linux distribution of your choice. I use Ubuntu, so this instruction refers to Ubuntu 18.04 LTS (with vanilla GNOME). Commands below should work on any Debian-based distribution, though. If you are using another distribution, some commands have to be adjusted accordingly.
2. Install SNAP Toolbox MAKE SURE IT IS VERSION 6.0
    1. in terminal: cd Downloads
    2. in terminal: chmod +x esa-snap_sentinel_unix_6_0.sh
    3. in terminal: ./esa-snap_sentinel_unix_6_0.sh
    4. When it Asks to configure python make sure to check no.
3. Install Python
    1. Go to https://www.anaconda.com/download/ and download Anaconda2 for linux.
    2. in terminal: bash ~/Downloads/Anaconda2-5.1.0-Linux-x86_64.sh
    3. agree the license terms
    4. choose an installation folder
    5. anaconda installation to PATH environment
4. Configure snappy SNAP – Python interface
    1. in terminal: sudo apt-get update
    2. in terminal: sudo apt-get install python-jpy
    3. in terminal: cd <snap-install-dir>/bin
    4. in terminal:./snappy-conf /home/<user>/anaconda2/bin/python
    5. if it works, go to /home/<user>/.snap/snap-python/ and copy the snappy folder to the site-package folder of your python installation /home/<user>/anaconda2/lib/python2.7/site-packages/
    6. To test if all is right, call spyder: in terminal: spyder
    7. Run this script in spyder:
       from snappy import ProductIO
       p = ProductIO.readProduct('/home/<user>/.snap/snap-python/snappy/testdata/MER_FRS_L1B_SUBSET.dim')
       list(p.getBandNames())
    8. • your output should look like this:
    [‘radiance_1’, ‘radiance_2’, ‘radiance_3’, ‘radiance_4’, ‘radiance_5’, ‘radiance_6’, ‘radiance_7’, ‘radiance_8’, ‘radiance_9’, ‘radiance_10’, ‘radiance_11’, ‘radiance_12’, ‘radiance_13’, ‘radiance_14’, ‘radiance_15’, ‘l1_flags’, ‘detector_index’]

5. Triangle
    1. In Terminal: sudo apt-get update
    2. In Terminal sudo apt-get install triangle-bin
6. Pygeoj

    1. In Terminal: pip install pygeoj
7. Sentinelsat
    1. In terminal: sudo apt-get install python-pip
    2. In terminal: pip install sentinelsat
8. Matlab
    1. This is the only not free available software in the whole workflow. Due to different licensing options and the good documentation how to install Matlab, this is skipped in this tutorial.
9. Snaphu
    1. In terminal: sudo apt-get update
    2. In terminal: sudo apt-get install snaphu
10. Csh
    1. In terminal: sudo apt-get install csh
11. StaMPS
    1. Got to https://homepages.see.leeds.ac.uk/~earahoo/stamps/, here you can find the handbook and the download link.
    2. Download the .tar.gz from the StaMPS homepage
    3. In Terminal: mv /home/<user>/Downloads/StaMPS_v3.3b1.tar.gz /home/<user>/
    4. In Terminal: tar -xvf StaMPS_v3.3b1.tar.gz
    5. In Terminal: cd StaMPS_v3.3b1/src
    6. In Terminal: make
    7. In Terminal: make install
    8. In Terminal: cd /home/<user>
    9. In Terminal: rm StaMPS_v3.3b1.tar.gz
12. Snap2stamps
    1. Download snap2stamps; preferably clone the git repository:
    2. In terminal: git clone https://github.com/mdelgadoblasco/snap2stamps.git
13. Configuration
    1. After the installation is complete, the StaMPS_CONFIG.bash file must be prepared to configure StaMPS on your machine. Be sure Matlab, snaphu, triangle and csh are installed.
    2. You should get an output similar to this, but remember the paths for your system.
        matlab: /usr/local/bin/matlab
        snaphu: /usr/bin/snaphu /usr/share/man/man1/snaphu.1.gz
        triangle: /usr/bin/triangle
        csh: /bin/csh /usr/share/man/man1/csh.1.gz
    3. The task of StaMPS_CONFIG.bash is to extend your PATH variable, so that your machine finds all these applications and some more directories which are used in StaMPS. Open StaMPS_CONFIG.bash with scite or some other text editor. You will notice that the configuration is prepared to point to much more applications and directories. Hence the preprocessing will be performed in SNAP, DORIS for instance, will never be used in our setting. We are able to comment a lot of the script. If you followed the installation guide in this summary, you can use the script below,

adapting the user in each path to your user name. In case your installation of snaphu or one of the other applications is not located in /usr/local/bin/ or /usr/bin/ you can set the path to the folder containing the application bin, using one of the prepared rows which are commented in my version. Do not miss the last line, where the unneeded variables are excluded from the final export to PATH. Notice, that the path information /usr/local/bin/ and /usr/bin/ are already part of PATH, hence we do not have to point to special folders containing snaphu or triangle, because they are installed in the default paths mentioned.

4. In your StaMPS_CONFIG.bash file edit the following lines: Make sure to add the # symbol to the corresponding lines to comment them out.

```
export STAMPS="/home/<user>/StaMPS_v3.3b1"
#export SAR="/home/<user>/ROI_PAC_3_0"
#export GETORB_BIN="/home/<user>/getorb/bin"
#export SAR_ODR_DIR="/home/<user>/SAR_FILES/ODR"
#export SAR_PRC_DIR="/home/<user>/SAR_FILES/PRC"
#export VOR_DIR="/home/<user>/SAR_FILES/VOR"
#export INS_DIR="/home/<user>/SAR_FILES/INS"
#export DORIS_BIN="/home/<user>/doris_v4.02/bin"
#export TRIANGLE_BIN="/home/<user>/triangle/bin"
#export SNAPHU_BIN="/home/<user>/snaphu-v1.4.2/bin"
#export ROI_PAC="$SAR/ROI_PAC"
# ROI_PAC VERSION 3
#export INT_BIN="$ROI_PAC/INT_BIN"
#export INT_SCR="$ROI_PAC/INT_SCR"
# ROI_PAC VERSION 2.3 and before
#set MACH=`uname -s`
#if ($MACH == "HP-UX") then
#  export ARCHC=HP
#else if ($MACH == "IRIX") then
#  export ARCHC=SGI
#else if ($MACH == "SunOS") then
#  export ARCHC=SUN
#else if ($MACH == "Linux") then
#  export ARCHC=LIN
#else if ($MACH == "Darwin") then
#  export ARCHC=MAC
#export INT_LIB="$ROI_PAC/LIB/$ARCHC"
#export INT_BIN="$ROI_PAC/BIN/$ARCHC"
#export FFTW_LIB="$SAR/FFTW/$ARCHC""_fftw_lib"
# shouldn't need to change below here
#export MY_BIN="$INT_BIN"
export MATLABPATH=$STAMPS/matlab:`echo $MATLABPATH`
#export DORIS_SCR="$STAMPS/DORIS_SCR"
```

Needed for ROI_PAC (a bit different to standard
export LC_NUMERIC="en_US.UTF-8"
export LC_TIME="en_US.UTF-8"
#export MY_SAR="$SAR"
#export OUR_SCR="$MY_SAR/OUR_SCR"
#export MY_SCR="$STAMPS/ROI_PAC_SCR"
export SAR_TAPE="/dev/rmt/0mn"
#export:PATH=${PATH}:$STAMPS/bin:$MY_SCR:$INT_BIN:$INT_SCR:$OUR_SCR:$DORIS_SCR:$GETORB_BIN:$DORIS_BIN:$TRIANGLE_BIN:$SNAPHU_BIN
export PATH=${PATH}:$STAMPS/bin:$MATLABPATH

5. In terminal: source /home/<user>/StaMPS-4.1-beta/StaMPS_CONFIG.bash
6. In terminal: printenv PATH
   Output should be something like:
   /home/<user>/anaconda2/bin:/usr/local/sbin:/usr/local/bin:/usr/sbin:/usr/bin:/sbin:/bin:/usr/games:/usr/local/games:/snap/bin:/home/<user>/StaMPS_v3.3b1/bin:/home/<user>/StaMPS_v3.3b1/matlab:
7. Add: source /home/<user>/StaMPS-4.1-beta/StaMPS_CONFIG.bash to your ~.bashrc file.

Snap2stamps workflow

The following steps are needed and provided by snap2stamps:

1. Sort the slave images in separated folders corresponding to their acquisition time.
2. Slave splitting (and slice assembling if needed) and annotated orbits replacement with Precise/Restituted Orbits.
3. Coregistration and interferogram generation done per slave and subswath. Here auxiliary files as DEMs and subset using a bounding box is performed. Both amplitude coregistered master-slave stack and interferogram with elevation and orthorectified latitude and longitude coordinates are saved as output.
4. StaMPS export is done providing for each pair coregistered stack and interferogram generated StaMPS compatible products.

snap2stamps contains the following files:

1. project.conf – file with parameters and paths needed for the processing
2. slaves_prep.py – script for sorting slaves into the expected folder structure
3. splitting_slaves_logging.py – script for slave splitting (and assembling if needed) and orbit correction
4. coreg_ifg_topsar.py – script for master-slave coregistration and interferometric generation
5. stamps_export.py – script for ouput data generation in StaMPS compatible format for PSI processing
6. Note that snap2stamps requires Python 2.7.

SNAP Steps:

1. Before starting make sure to go to your SNAP directory -> bin -> gpt.vmoptions

2. Change the -xmx value to 60-75% of your systems ram. SNAP uses a large amount of ram so I recommend your system having at least 32gb.
3. Select optimal master in SNAP using Radar / Interferometric / InSAR Stack Overview
4. Perform subsetting of whole image using TOPSAR Split via Radar / Sentinel-1 TOPS / S-1 TOPS Split. Set the processing parameter
    1. subswath (IW 1-3),
    2. polarization (vertical sent, vertical returned – VV), and
    3. bursts (using the bursts-slider) in the respective tab.
5. Get LAT/LON MIN/MAX (bounding box) for PSI area of interest. This can be done in snap by opening one of your split files. Right click on the image and select spatial subset from view -> geographic coordinates.
6. Create a project folder where you will store your sentinel scenes for the snap2stamps steps. You will need to make two folders, "master" and "slaves".
7. Add both the original zip file of the scene to master as well as the split zip and split.dim
8. Add all of the slave zips to your slaves folder.
9. Now go to your snap2stamps directory and go to bin. Open project.conf and edit it accordingly. It should be similar to this:

    CONFIGURATION FILE
    # PROJECT DEFINITION
    PROJECTFOLDER=/media/sf_Shared/Project
    GRAPHSFOLDER=/home/mhaley/Work/snap2stamps/graphs
    # PROCESSING PARAMETERS
    #IW1=IW2
    MASTER=/media/sf_Shared/Project/master/S1A_IW_SLC_1SDV_20180407T003356_20180407T003423_021354_024C0E_BAD9_split.dim
    # AOI BBOX DEFINITION
    LONMIN=-97.119
    LATMIN=26.9
    LONMAX=-97.732
    LATMAX=27.745
    # SNAP GPT
    GPTBIN_PATH=/home/mhaley/Pysnap1/bin/gpt
    # COMPUTING RESOURCES TO EMPLOY
    CPU=8
    CACHE=32G

Snap2stamps scripts

Run the following python scripts to prepare your files for stamps. Make sure to change your directory to your snap2stamps/bin folder.

1. Slave sorting.
    1. In terminal: python slaves_prep.py project.conf
    2. This step is only to set up directories, very fast.
2. slave splitting and orbit correction
    1. in terminal: python splitting_slaves.py project.conf
    2. This step splits the slaves to the same area as the masters and applies orbital corrections. ~ 20 mins per scene.
3. master-slave coregistration and interferometric generation
    1. in terminal: python coreg_ifg_topsar.py project.conf
    2. This is the interferogram generation step. Be careful how large your AOI is as this step is very RAM intensive and time consuming.
4. ouput data generation in StaMPS compatible format
    1. in terminal: python stamps_export.py project.conf
    2. creates a INSAR_<Master Date> folder that stamps will use. ~1hr per scene.
5. This is the final step before using StaMPS in the matlab interface.
    1. mt_prep_snap <your master date> /<Path to your project folder/INSAR_MASTERDATE/ 0.4(Amplitude dispersion, increasing this value will exclude noisy points.)
    2. note, you can also cut AOI into patches to lessen computer workload by adding two values after the amplitude dispersion so your input will now look similar to this if you wanted 4 rows and 4 columns of patches:
    3. mt_prep_snap <your master date> /<Path to your project folder/INSAR_MASTERDATE/ 0.4 4 4
    4. here is an example that I used: mt_prep_snap 20180218 /media/sf_ShareC/Project1/INSAR_20180218/ 0.4

StaMPS Workflow

In terminal: matlab

1. try getparm command in the matlab window. A list of parameters should be returned, if not, check section Configuration and your PATH variable.
2. Now it is more or less technically ‘easy’ to analyse PS with StaMPS.
3. You are able to run stamps by typing into the matlab command window: stamps(x, y) where x is the first step and y is the last step of stamps you would like to run. Alternatively you can run it step by step by using stamps(x,x).
4. If you would like stamps to run from the last completed step you can enter stamps(0,x)
5. To change a parameter type into the matlab window: setparm(‘parametername’, value)

1. Loading Ps candidates
    1. Stamps(1,1)
    2. Once step 1 has been run details can be listed for each ifg by using ps_info

2. Step 2 Calculate temporal coherence by estimating phase noise
    1. stamps(2,2)
    2. Important parameters: max_topo_error, filter_grid_size, filter_weighting, clap_win,clap_low_pass_wavelength, clap_alpha, gamma_max_iterations
3. PS selection
    1. stamps(3,3)
    2. important parameters: select_method, density_rand, percent_rand
4. PS weeding\
    1. stamps(4,4)
    2. important parameters: weed_standard_dev, weed_max_noise, weed_neighbours.
5. Phase correction
    1. stamps(5,5)
    2. important parameters: merge_resamples_size, merge_standard_dev
6. Phase unwrapping
    1. stamps(6,6)
    2. important parameters: unwrap_grid_size, unwrap_gold_alpha, unwrap_prefilter_flag, unwrap_time_win
7. Estimate spatially-correlated look angle error
    1. stamps(7,7)
    2. important parameters: scla_deramp, drop_ifg_index
8. Atmospheric filtering
    1. stamps(8,8)
    2. important parameters: scn_wavelength, scn_time_win
    3. If you would like to use TRAIN for weather corrections please refer to the TRAIN manual located at https://github.com/dbekaert/TRAIN/blob/master/manual/TRAIN_manual.pdf
9. Plotting
    1. Ps_plot(‘v-do’) – to plot with velocity minus d which are SCLA errors, and o phase ramps. Can use other combinations such as ‘v-d’, ‘v-o’ etc.
    2. If you want to see a time series of the selected points you can plot as follows, ps_plot(‘v-do’, ‘ts’)
10. Exporting the time series points to a csv file
    1. Make sure to plot with the TS flag first. Example: ps_plot(‘v-do’, ‘ts’)
    2. Enter the following blocks of text into the matlab console sequentially.
    1. load parms.mat;
       ps_plot('v-do', -1);
       load ps_plot_v-do.mat;
       lon2_str = cellstr(num2str(lon2));
       lat2_str = cellstr(num2str(lat2));
       lonlat2_str = strcat(lon2_str, lat2_str);
    2. lonlat_str = strcat(cellstr(num2str(lonlat(:,1))), cellstr(num2str(lonlat(:,2))));
       ind = ismember(lonlat_str, lonlat2_str);
    3. disp = ph_disp(ind);

```
disp_ts = ph_mm(ind,:);
export_res = [lon2 lat2 disp disp_ts];
```

4.
```
metarow = [ref_centre_lonlat NaN transpose(day)-1];
k = 0;
export_res = [export_res(1:k,:); metarow; export_res(k+1:end,:)];
export_res = table(export_res);
writetable(export_res,'stamps_tsexport.csv')
```